

Direct Numerical Simulation of Turbulent Pipe Flow at Moderately High Reynolds Numbers

George K. El Khoury · Philipp Schlatter ·
Azad Noorani · Paul F. Fischer · Geert Brethouwer ·
Arne V. Johansson

Received: 22 October 2012 / Accepted: 19 June 2013 / Published online: 10 July 2013
© Springer Science+Business Media Dordrecht 2013

Abstract Fully resolved direct numerical simulations (DNSs) have been performed with a high-order spectral element method to study the flow of an incompressible viscous fluid in a smooth circular pipe of radius R and axial length $25R$ in the turbulent flow regime at four different friction Reynolds numbers $Re_\tau = 180, 360, 550$ and 1,000. The new set of data is put into perspective with other simulation data sets, obtained in pipe, channel and boundary layer geometry. In particular, differences between different pipe DNS are highlighted. It turns out that the pressure is the variable which differs the most between pipes, channels and boundary layers, leading to significantly different mean and pressure fluctuations, potentially linked to a stronger wake region. In the buffer layer, the variation with Reynolds number of the inner peak of axial velocity fluctuation intensity is similar between channel and boundary layer flows, but lower for the pipe, while the inner peak of the pressure fluctuations show negligible differences between pipe and channel flows but is clearly lower than that for the boundary layer, which is the same behaviour as for the fluctuating wall shear stress. Finally, turbulent kinetic energy budgets are almost indistinguishable between the canonical flows close to the wall (up to $y^+ \approx 100$), while substantial differences are observed in production and dissipation in the outer layer. A clear Reynolds number dependency is documented for the three flow configurations.

Keywords Wall turbulence · Pipes · Channels · Boundary layers · Direct numerical simulation

G. K. El Khoury (✉) · P. Schlatter · A. Noorani · G. Brethouwer · A. V. Johansson
Linné FLOW Centre and Swedish e-Science Research Centre (SeRC),
KTH Mechanics, Royal Institute of Technology, 100 44 Stockholm, Sweden
e-mail: georgeek@mech.kth.se

P. F. Fischer
MCS, Argonne National Laboratory, 9700 S. Cass Avenue, Argonne, IL 60439, USA

1 Introduction

There has been a long-standing tradition to study the flow of a viscous fluid close to a solid surface. Ludwig Prandtl in the early twentieth century highlighted the effect of viscosity close to the walls by introducing the concept of boundary layers. These boundary layers are ubiquitous in engineering applications since in most systems the fluid motion is in contact with solid surfaces such as in the flow of air around an airplane wing or that of water around a submarine. It is thus hardly surprising that wall-bounded flows have attracted considerable interest among researchers. Of particular importance in such flows is the near-wall region since a large fraction of the drag of immersed streamlined moving bodies stems from this thin layer directly adjacent to surfaces. The internal dynamics of these regions is still far from understood; open questions relate e.g. to the scaling behaviour at higher Reynolds numbers in addition to the possibility of accurate modelling.

When it comes to wall-bounded flows, there are three simple geometrical configurations which are referred to as the canonical cases: the spatially evolving boundary layer, the channel and the pipe. Most of the early studies in this area were conducted by means of experiments. Only recently, computer power has grown sufficiently large to attempt fully resolved numerical solutions of all relevant turbulent scales. The direct numerical simulation (DNS), albeit simple in spirit, has proven extremely valuable in obtaining new insights in this context. The first DNS of channel flow was by Kim et al. [15] and of boundary layers by Spalart [31]. These two flow cases have been studied extensively using DNS in the past years; see e.g. Jiménez and Hoyas [13] and Schlatter and Örlü [27]. Pipe flow, on the other hand, is the only canonical flow case that has not yet been thoroughly studied by DNS. One of the characteristic features of a pipe is its enclosed geometry, as opposed to boundary layers and channels, which makes it the easiest to realise in experiments in comparison to the latter two cases, as no side-wall effects are to be taken into consideration. On the numerical side, however, the fact that the governing Navier–Stokes equations tend to be formulated in cylindrical coordinates in order to express the fluid motion in axisymmetric configurations results in an apparent numerical singularity at the centreline. This essentially made channels the most straightforward configuration for DNS as the mesh in this case is trivial, and very well described by the standard Fourier–Chebyshev (Gauss–Lobatto) distribution. It is worthwhile to note that the numerical singularity at the pipe axis can be avoided for instance by choosing an even number of Gauss–Lobatto collocation points in the radial direction, and thus no collocation point would be present along the pipe centreline.

The first well-resolved DNS on turbulent pipe flow was performed by Eggels et al. [8] who considered a pipe of length $10R$ at a diameter-based bulk Reynolds number (Re_b) of 5,300. This corresponded to a friction Reynolds number of 180, also referred to as Kármán number $Re_\tau = R^+ = u_\tau R/\nu$, and was obviously motivated by the pioneering work of Kim et al. [15] on turbulent channel flow. Here, u_τ is the friction velocity, R is the pipe radius and ν is the kinematic viscosity. In their work, Eggels et al. conducted a comparative study between the two canonical wall-bounded flows and found that the mean axial velocity profile in a pipe, at such low Reynolds number, does not follow the log-law in contrast to channels. During the following decade, an increasing number of numerical studies were performed on pipe flows by Orlandi and Fatica [25], Wagner et al. [33] and Fukagata and Kasagi [10]. Although

these works were insightful, they were mainly at low Reynolds numbers and mostly confined to low order numerical methods. The highest Reynolds number, in this case, was $Re_\tau = 320$ by Wagner et al. in a pipe of length $10R$. More recently, Walpot et al. [34] performed a DNS of flow in similarly short pipes ($10R$) with a spectral method, based on Fourier–Galerkin and Chebyshev collocation formulations, at $Re_b = 5,300$ and $10,300$.

In pipe flows, the only geometrical parameter to be chosen is its axial length. An insufficient domain length simply leads to inaccurate results since it limits the maximum length of structures in the flow. In recent experimental studies, (very) large-scale motions (VLSM and LSM), with lengths of $5R$ up to $20R$, R is the pipe radius, have been found in fully developed turbulent pipe flow in the outer region of the boundary layer; see e.g. Kim and Adrian [16]. These structures, being strongest in the outer region, even leave their footprint quite close to the wall and in the log layer; Guala et al. [11], Monty et al. [21] and Schlatter et al. [29]. These large-scale structures are very energetic and active; i.e. they contribute to the Reynolds shear stress. Large-scale motions thus play an important role in the dynamics of turbulent pipe flows, and need to be captured accordingly, implying that the computational domain needs to be sufficiently long.

In recent years, pipe-flow experiments have been pushed to very high Reynolds numbers mostly by the pressurised so-called “Superpipe” located in Princeton; see Zagarola and Smits [37]. Considerable interest in high Re pipe flows stems from the still many open question relating to the scaling of turbulent statistics as reviewed by Marusic et al. [20] and Smits et al. [30]. For instance, it has been argued in the past that the peak of the root-mean-square (rms) of the axial/streamwise velocity fluctuations is nearly constant as a function of the Reynolds number, however, no conclusive support has been found. In addition, some measurements indicate the appearance of an “outer” peak in the rms, which is also actively debated; see e.g. Alfredsson et al. [1]. The need for reliable turbulent pipe flow experiments at high Reynolds numbers, like the CICLoPE project, was addressed by Talameli et al. [32]. DNS of pipe flow, on the other hand, have only recently become the focus of increased attention with the work by Wu and Moin [36]. In that study, the authors used a second order finite difference method to study the turbulence in a pipe of axial length $15R$ at a bulk-diameter based Reynolds number of $Re_b = 44,000$; friction Reynolds number of $Re_\tau = 1,142$. Chin et al. [5] and Klewicki et al. [17], on the other hand, used a high-order spectral/spectral element DNS code to study the influence of pipe length on turbulence statistics and the evolution of the mean momentum fields at friction Reynolds numbers of 170, 500 and 1,000. The authors concluded that a pipe length of $25R$ is sufficiently long to capture all the relevant structures present in pipe flow up to $Re_\tau = 1,000$. Other DNS studies on pipes were done by Boersma [2], and more recently by Wu et al. [35] at $Re_\tau = 685$ with a $30R$ long pipe in order to investigate the existence of very large-scale motions.

Essentially, one would expect that various simulations and experiments on pipe flows, once the axial extent is chosen sufficiently large, agree well with each other. However, in spatially developing turbulent boundary layers, a recent comparison between a number of available simulation data sets by Schlatter and Örlü [27] has shown a surprisingly large spread of the data even for basic quantities such as the shape factor and friction coefficient, indicating that not even the mean profiles agreed between the various DNS. Most of these discrepancies could be traced back to

differences in the way turbulence is introduced in the domain (tripping, recycling) as discussed by Schlatter and Örlü [28]. It is therefore interesting to see whether the expected close agreement of DNS data in pipe can be confirmed based on the available literature data, and to what extent these data agree with corresponding simulations in channel and boundary-layer geometries. It is thus the purpose of this paper to critically assess the available DNS data for pipes, channels and boundary layers, and try to find out which differences or correspondence between the data sets are real and caused by physics, and which discrepancies are likely caused by the numerics. Therefore, in a first step our new simulations, which were obtained in reasonably long pipes with high accuracy in terms of resolution and convergence order of the method, are described. After presenting the basic statistics, including data for the mean and fluctuating pressure, the focus is shifted to more detailed investigation of the data. A number of sensitive observables, such as the statistical moments at the pipe centre or the deviations of the mean profile from analytical composite profiles, are discussed, and the respective discrepancies are highlighted. Finally, energy budgets of the turbulent flow in pipes are presented and put into perspective with the other canonical wall flows.

2 Governing Equations and Numerical Method

We consider the pressure-driven incompressible flow of a viscous Newtonian fluid in a smooth circular pipe where the governing equations are the time-dependent Navier–Stokes equations given by

$$\nabla \cdot \mathbf{u} = 0, \quad (1)$$

$$\frac{\partial \mathbf{u}}{\partial t} + (\mathbf{u} \cdot \nabla) \mathbf{u} = -\nabla p + \frac{1}{Re_b} \nabla^2 \mathbf{u}. \quad (2)$$

Here, Re_b is the bulk Reynolds number defined as $U_b D/\nu$ where D is the pipe diameter, U_b is the mean bulk velocity and ν is the kinematic viscosity.

The DNS code used to numerically solve Eqs. 1 and 2 is *nek5000*; developed by Fischer et al. [9]. *Nek5000* is a computational fluid dynamics solver based on the spectral element method (SEM) that is well known for its (spectral) accuracy, favourable dispersion properties, and efficient parallelisation. In *nek5000*, the incompressible Navier–Stokes equations are solved using a Legendre polynomial based SEM. These equations are cast into weak form and discretised in space by the Galerkin approximation. The basis chosen for the velocity space are typical N th-order Lagrange polynomial interpolants on Gauss–Lobatto–Legendre (GLL) points whereas for the pressure space, on the other hand, Lagrangian interpolants of order $N - 2$ are used on Gauss–Legendre quadrature points. This is what is formally known as the $\mathbb{P}_N - \mathbb{P}_{N-2}$ SEM and was formulated by Maday and Patera [19]. It is worthwhile to note that the $\mathbb{P}_N - \mathbb{P}_N$ formulation is also implemented in *nek5000* but has not been used in the present work. The time-stepping in *nek5000* is semi-implicit in which the viscous terms of the Navier–Stokes equations are treated implicitly using third-order backward differentiation (BDF3), whereas the non-linear terms are treated by a third order extrapolation (EXT3) scheme. This leads to the following system for the basis coefficient vectors to be solved at every time step

$$H \underline{\mathbf{u}}^{n+1} = D^T \underline{\mathbf{p}}^{n+1} + B \underline{\mathbf{f}}^{n+1}, \quad D \underline{\mathbf{u}}^{n+1} = 0. \quad (3)$$

Here, D is the discrete divergence operator, while $H = Re_b^{-1}A + \beta_0/\Delta t B$ is the discrete equivalent of the Helmholtz operator, $-Re_b^{-1}\nabla^2 + \beta_0/\Delta t$, with discrete Laplacian A and mass matrix B associated with the velocity mesh. $\beta_0 = 11/3$ is the coefficient associated with BDF3 and \int^{n+1} accounts for the remaining BDF3 terms as well as the extrapolated nonlinear terms and the body force, which is determined implicitly to satisfy a fixed flow rate.

The solution obtained from `nek5000` for the Navier–Stokes equations is in a Cartesian coordinate system whose origin is located at the pipe centre at an axial position of zero; $z = 0$. The velocity vector is thus $\underline{u} = (u, v, w)$ in (x, y, z) . Accordingly, the singularity, found along the centreline of the pipe when the Navier–Stokes are expressed in cylindrical coordinate, does not occur in the present formulation. The various statistical quantities calculated on-the-fly during the simulation are averaged in time and axial direction only. Subsequently, we are left with statistical data that is two-dimensional on a grid similar to that shown in Fig. 1. Afterwards, spectral interpolation is employed in order to preserve the simulation accuracy and to pass from the 2D-SEM grid to a regular (r, θ) cylindrical grid. Here, the spacing is taken equidistant in the azimuthal direction allowing Fourier differentiation whereas in the radial direction a non-uniform grid together with compact finite difference scheme is used. The spacing in the latter direction is chosen in such a way that the original grid spacing near the wall is preserved. In a final postprocessing step, the first, second and third order moments in addition to the velocity gradient as well as the Reynolds-stress budgets terms are calculated with respect to a cylindrical system by means of appropriate tensor rotations.

In the present study, the computational domain consists of a circular pipe of radius R and length $25R$ with the pipe axis taken along the axial z -direction. The flow in the axial direction is driven by a pressure gradient, which is adjusted dynamically by the time-integration scheme to assure a constant mass flux is obtained. This method is used instead of a fixed pressure gradient. The basic idea is that the mean-flow is linear in the pressure gradient, which allows the latter parameter to be adjusted in each time step in order to maintain a constant bulk velocity U_b . From the force balance, the

Fig. 1 Cross-sectional view of a quarter-section of the computational mesh for the simulation at $Re_\tau = 550$. Both the element boundaries and the Gauss–Lobatto–Legendre quadrature points ($N = 7$) are clearly visible

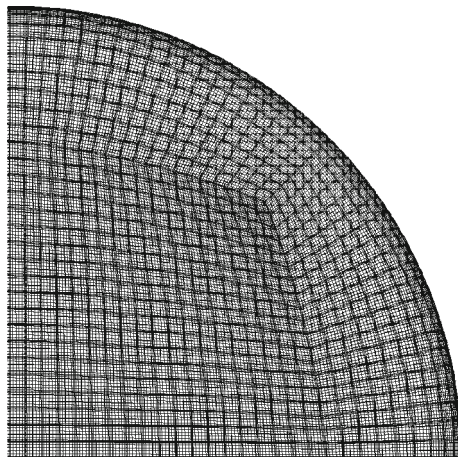


Table 1 Details on the present turbulent pipe flows simulations

| Re_b | # of elements | # grid points | Δr^+ | $\Delta R\theta^+$ | Δz^+ |
|--------|---------------|---------------------|--------------|--------------------|--------------|
| 5,300 | 36,480 | 18.67×10^6 | (0.14, 4.44) | (1.51, 4.93) | (3.03, 9.91) |
| 11,700 | 237,120 | 121.4×10^6 | (0.16, 4.70) | (1.49, 4.93) | (3.03, 9.91) |
| 19,000 | 853,632 | 437.0×10^6 | (0.15, 4.49) | (1.45, 4.75) | (3.06, 9.99) |
| 37,700 | 1,264,032 | 2.184×10^9 | (0.15, 5.12) | (0.98, 4.87) | (2.01, 9.98) |

mean pressure gradient is related to the wall shear stress as $-(dP/dz)^+ = 2(l^*/R) = 2 \times 10^{-3}$ for $Re_\tau = 1,000$. The measured rms fluctuations of the pressure gradient $(dP/dz)_{rms}^+$ are approximately 1.3×10^{-5} at the same Re_τ .

Figure 1 shows a cross-sectional view of a quarter-section of the spectral element mesh used in a current turbulent pipe flow simulation for $Re_\tau = 550$. Here, a total of 28 spectral elements is used on the horizontal and vertical axis of Fig. 1, respectively. Inside each element the nodes are distributed using Gauss–Lobatto–Legendre (GLL) points. With the polynomial order set to 7, the total number of grid points is approximately 437 million at this Reynolds number. For all the direct numerical simulations presented in the current study the grid spacing, measured in wall units, is set such that $\Delta r_{max}^+ \leq 5$ with four and fourteen grid points placed below $\Delta r^+ = 1$ and 10 (from the wall), respectively, and $\Delta R\theta_{max}^+ \leq 5$ and $\Delta z_{max}^+ \leq 10$. The details of the computational meshes at the various Reynolds numbers are presented in Table 1.

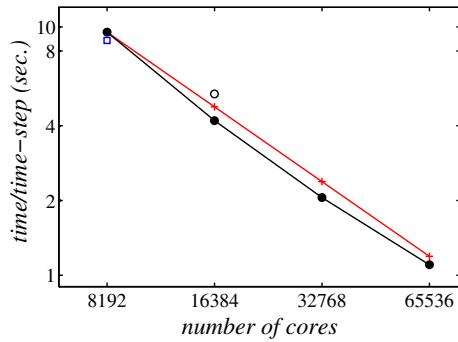
3 Parallel Scaling of nek5000

This section provides information about the parallel efficiency and scaling properties of nek5000 used in the current simulations. The hardware utilised for the present computations is Lindgren located at PDC (Stockholm) and HECToR at EPCC (Edinburgh). Both systems are Cray XE6 systems where the compute nodes are interconnected by a 3D-torus Gemini network. Lindgren consists of 1516 compute nodes where each node has two 12-core AMD Opteron 2.1 GHz processors and 32 GByte memory. This amounts to a total of 36,384 cores with 24 cores per node and a theoretical peak performance of 8.4 GFlop per core. HECToR, on the other hand, has 2816 compute nodes with two 16-core AMD Opteron 2.3GHz Interlagos processors per node and 32 GByte memory. The total number of cores is thus 90,112 and the theoretical peak performance is 9.2 GFlop per core.

The data points in Fig. 2 show the wall time per time step for nek5000 as a function of the core count for the current simulations at $Re_b = 37,700$. At this Reynolds number a total of 1,264,032 spectral elements is used with the polynomial order set to 11. This gives a total number of grid points that is equal to 2.1842×10^9 . It is readily observed that there is a very efficient usage of the hardware by nek5000. There is a slightly super-linear speed-up of 113 % from 8,192 to 16,384 cores. The reason for this scaling behaviour can most probably be attributed to the fact that a part of the machine was used during the test, and thus the nodes were distributed over the whole machine. Meanwhile, the scaling is essentially linear between 16,384 to 32,768 cores whereas after this point and at a number of cores of 65,536 the curves depart from the linear scaling and we measure a slightly reduced parallel efficiency of 93 %.

Apart from the excellent parallel capabilities it is also interesting to compare the efficiency of the numerical method to other methods. Such a comparison is very

Fig. 2 Time per time step for $Re_\tau = 1,000$. HECToR (EPCC Edinburgh, UK): —●—, full node; ○, half node. Lindgren (PDC, Sweden): □, full node; —+—, linear scaling



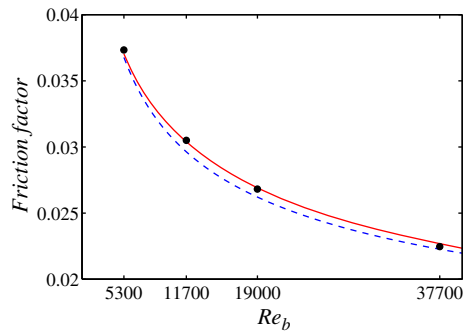
difficult, and will always mix aspects of implementation, architectures and specific choices of the numerics (order, time integration etc.). In Ohlsson et al. [24], *nek5000* was compared to the Fourier–Chebyshev method *Simson* [4] for plane channel flow at $Re_\tau = 180$. Assessing the effective accuracy of some observables (like wall shear stress), no particular difference between the code for the same number of degrees of freedom could be established. Furthermore, running strictly in serial mode the fully spectral method turned out to be about an order of magnitude faster when also taking into account the different time-step limitations due to the non-uniform grids. Note, however, that channel flow is ideally represented using a Fourier–Chebyshev method, and thus for the present case in pipe geometry the SEM would be more efficient.

4 Results

Perhaps one of the most important motivation to perform studies of pipe flows was the determination of the friction factor (f) or pressure drop in order to estimate the head loss. The latter quantity is defined as $\Delta p = f(L/D)(\rho V^2/2)$ where L and D are the length and diameter of the pipe respectively, ρ is the density and V is the mean velocity. f is a dimensionless parameter and mainly depends on the Reynolds number of the flow and ratio between the absolute roughness e and the pipe diameter D , formally known as the relative roughness. Several empirical equations have been given throughout the years by engineers in order to estimate f , and one of the best known charts for the determination of head loss is the Moody diagram [22]. In Fig. 3 the friction factor obtained from the present DNS, defined as $f = 8u_\tau^2/U_b^2$, is plotted against the estimates given by Blasius and Colebrook [22]. From the curves, it can be readily seen that the Blasius correlation gives the best estimates at low Reynolds number but fails at $Re_b = 37,700$, whereas the Colebrook correlation shows a good agreement with the present DNS at the highest Reynolds number, $Re_b = 37,700$.

Several integral quantities for the different Reynolds numbers are listed in Table 2. This includes the friction Reynolds number Re_τ , the Reynolds number based on centreline velocity Re_{cl} , the centreline velocity in wall units U_{cl}^+ , the friction velocity u_τ normalised by U_b and the shape factor H_{12} , defined as the ratio between the displacement thickness δ^* and momentum-loss thickness θ . In pipe flow the latter two quantities are given by $\delta^*(2R - \delta^*) = 2 \int_0^R r(1 - U_z/U_{cl}) dr$ and $\theta(2R - \theta) =$

Fig. 3 Friction factor f as a function of the bulk Reynolds number Re_b . •, *Present DNS*; —, *Blasius law*: $f = 0.316/Re^{0.25}$; - - -, *Colebrook law*: $1/\sqrt{f} = -2.0 \log[(e/D)/3.7 + 2.51/(Re\sqrt{f})]$; Here, e/D denotes the relative roughness of the pipe that is zero in the present case



$2 \int_0^R r (U_z/U_{cl}) (1 - U_z/U_{cl}) dr$. From Table 2 it can be seen that the shape factor, as expected, decreases with increasing Reynolds number.

4.1 Instantaneous velocity and vorticity

The change in character of the flow field with increasing Reynolds number is illustrated in Fig. 4 where instantaneous cross-sectional views of axial velocity are shown at one axial z -position. The general increase in the range of scales with increasing Reynolds number is evident throughout the cross-section, although the large scales dominate for all Reynolds numbers in the central region of the pipe. It is well known that the average spacing between near-wall low-speed streaks is about 100 wall units. For the lowest Re_τ studied here, that corresponds to about half a pipe radius. This is in accordance with the observed near-wall flow pattern in Fig. 4a. For the highest Re_τ studied here the streak spacing should be expected to be about a tenth of the pipe radius, which appears compatible with the pattern observed in Fig. 4d. Another cross-sectional view is shown in Fig. 5 where the instantaneous axial vorticity (ω_z) at $Re_b = 19,000$ is displayed together with its spectral element mesh used during the simulation with nek5000. Here, it can be clearly seen that the flow is dominated by strong vortical motion close to the walls where small intense counter-rotating vortices are observed. Accordingly, these vortices transport fluid from and to the wall region. In the outer region, on the other hand, the flow is dominated by a larger-scale motion. This figure also gives an indication about the quality of the spatial mesh resolution. At this Reynolds number a total of 2,964 spectral elements are used which gives around 1.9 million grid points in each circular cross-section with a polynomial order of 7. The pseudo-colours of ω_z are smooth across the element boundaries and there are no visible mesh effects due to discretisation by spectral element method. We can therefore conclude that the characteristics of the spatial

Table 2 Integral quantities and start time for averaging as a function of Re_b

| Re_b | Re_τ | Re_{cl} | U_{cl}^+ | u_τ/U_b | H_{12} | Start time T_S |
|--------|-----------|-----------|------------|--------------|----------|---------------------------|
| 5,300 | 181 | 3,464 | 19.13 | 0.0683 | 1.85 | $(1200U_b/R, 82u_\tau/R)$ |
| 11,700 | 361 | 7,443 | 20.60 | 0.0617 | 1.62 | $(310U_b/R, 19u_\tau/R)$ |
| 19,000 | 550 | 12,000 | 21.79 | 0.0579 | 1.55 | $(310U_b/R, 18u_\tau/R)$ |
| 37,700 | 1,000 | 23,406 | 23.43 | 0.0530 | 1.47 | $(210U_b/R, 11u_\tau/R)$ |

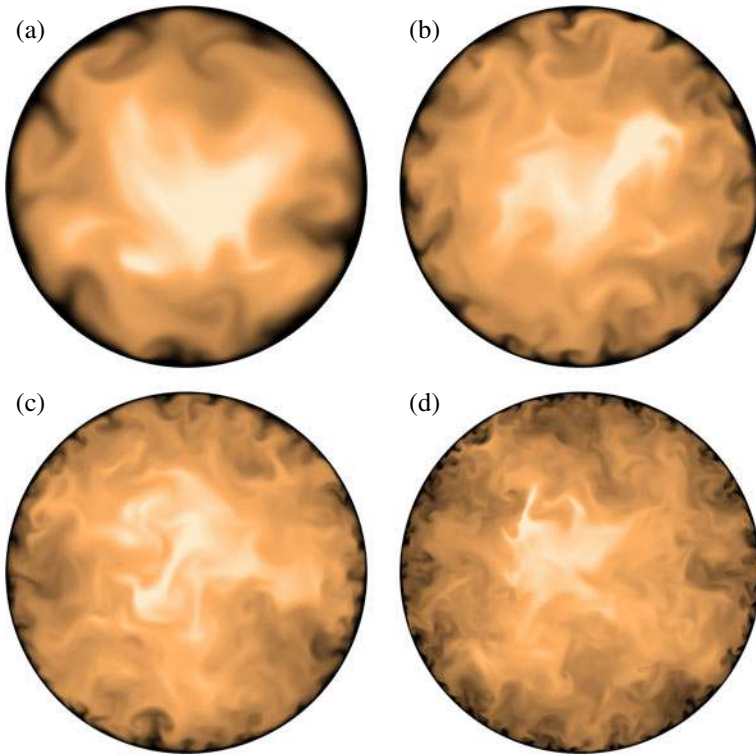


Fig. 4 Pseudo-colour visualisation of the instantaneous axial velocity u_z normalised by the bulk velocity U_b . **a** $Re_b = 5,300$; **b** $Re_b = 11,700$; **c** $Re_b = 19,000$; **d** $Re_b = 37,700$. Here, the colours vary from 0 (black) to 1.3 (white)

grid, discussed in Section 3, is fully appropriate for a high-quality DNS of turbulent pipe flow.

4.2 Mean statistics

The profiles of the mean axial velocity component from the present pipe flow simulations are shown in Fig. 6a together with the linear and logarithmic parts of the law of the wall. In the viscous sublayer for $y^+ = (1 - r)^+ < 5$, the profiles naturally adhere to $U_z^+ = y^+$, while at larger distances from the wall, for $y^+ > 30$, it is readily observed that the mean velocity profiles do not collapse onto one single curve. At $Re_b = 5,300$, U_z^+ deviates substantially from the log-law. This deviation is larger than that for plane channel and boundary layer flows at the same (low) Reynolds number. Such behaviour has also been reported by several previous works on pipe flow, as for example in Eggels et al. [8]. As the Reynolds number increases to 11,700, 19,000 and 37,700, U_z^+ shows a better agreement with the log-law. Here, we have used the standard values of $\kappa = 0.41$ and $B = 5.2$, although other values have been suggested for pipe flows. Finally, the profiles show a clear wake region as the pipe's centreline is approached, indicated by a distinct deviation from the log-law.

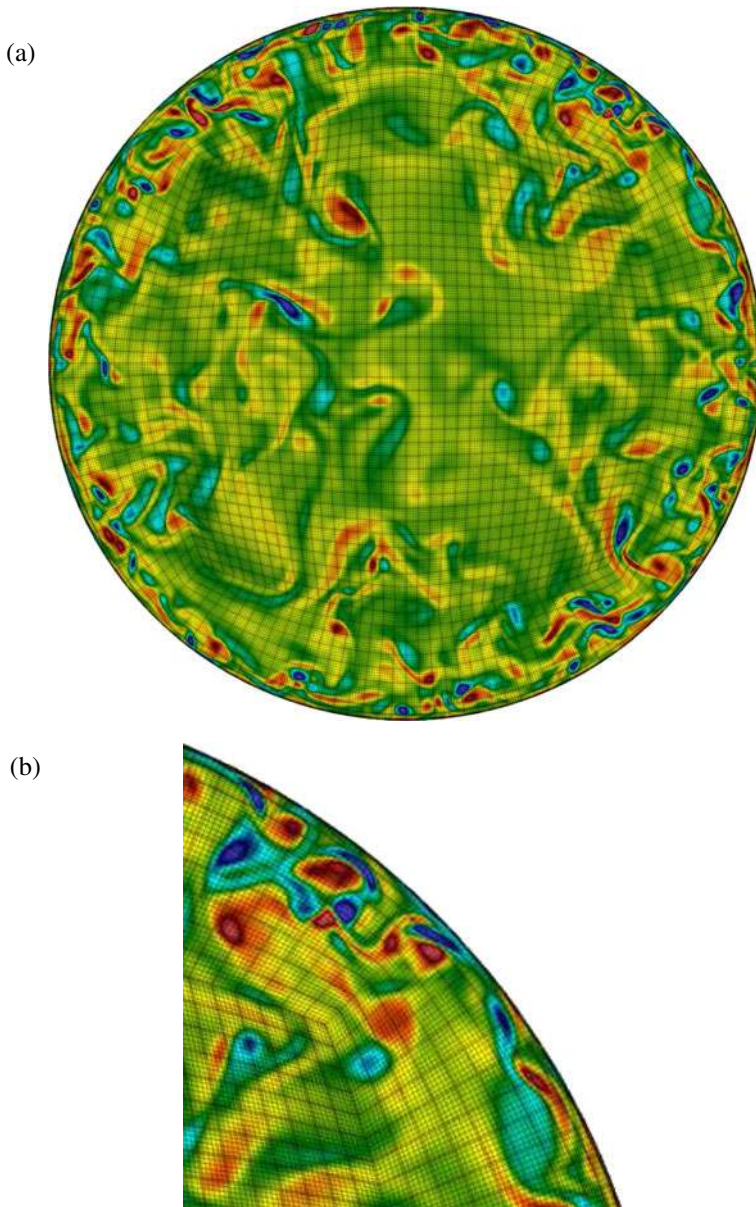


Fig. 5 **a** Pseudo-colours of the instantaneous axial vorticity ω_z for $Re_b = 19,000$ together with the spectral element boundaries. **b** Zoomed view of an upper right part of **a**

Figure 6b displays the mean axial velocity at $Re_\tau = 1,000$ together with the mean streamwise velocity U obtained from DNS of turbulent boundary layers [27] and plane channel flow [18] at approximately the same friction Reynolds number. Both DNSs were performed with the spectral code *Simson* [4] and a large computational domain. It is apparent that the profiles collapse well in the viscous sublayer and

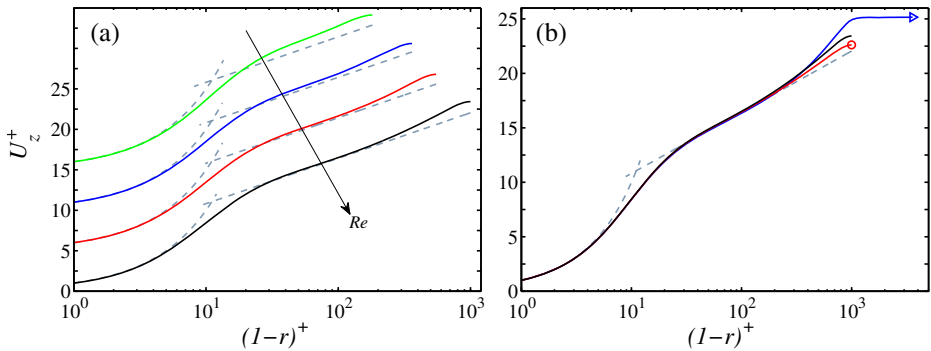


Fig. 6 **a** Profiles of mean axial velocity U_z^+ at $Re_b = 5,300, 11,700, 19,000$ and $37,700$ in inner scaling. **b** $Re_\tau \approx 1,000$. Pipe: —, present DNS; channel: —○, Lenaers et al. [18]; boundary layer: —△, Schlatter and Örlü [27]. $U_z^+ = (1-r)^+$ and $U_z^+ = \kappa^{-1} \ln(1-r)^+ + B$ with $\kappa = 0.41$ and $B = 5.2$ are given as dashed lines

log-law region and deviate from each other in the outer layer. As the wake region is approached, the turbulent boundary layer and channel profiles attain the highest and lowest scaled velocity values, respectively, with the pipe flow in between.

Jiménez et al. [14] studied extensively the behaviour of the velocity and pressure fluctuations in the outer layer of zero-pressure-gradient boundary layer and channel flows conducting detailed comparisons between the two. They reported that the pressure fluctuations are stronger in the outer layer of boundary layers due to the intermittency between the potential and rotational flow regions. Accordingly, this results in a higher mean velocity in the wake region for boundary layers. Nagib and Chauhan [23] looked at the Coles wake parameter Π [6] in order to study the mean and large-scale outer structures in pipes, channels and boundary layers. In their work, the authors considered a large data set with a wide range of Reynolds number and reported that the wake parameter was highest in boundary layers and lowest in channels in agreement with our results. While the higher value of Π in the boundary layer was due to its spatial development and interaction with the outer region, the origin of the difference between channel and pipe is still unclear.

Another Reynolds-number effect in turbulent pipe and other wall-bounded flows is in the variation of the axial/streamwise turbulence intensity with the Reynolds number. This is shown in Fig. 7a in wall units for the present pipe DNS. It is easy to see that in the viscous sublayer the profiles collapse well although it is clear that the inner scaling does not hold for larger wall distances where substantial discrepancies in the profiles are observed for $(1-r)^+ > 20$. In particular, the peak in $u_{z,rms}^+$ is seen to increase slightly with Re_τ and the maximum is consistently located around $y^+ = 15$ as in the case of channel and boundary layers. This increase is related to the growing importance of large structures with increasing Re_τ , leaving their footprint at the wall [7]. At the pipe centre, on the other hand, the values of $u_{z,rms}^+$ reach approximately the same values for the pipe flow and are in good agreement with channel flow. The maximum of inner scaled radial and azimuthal turbulence intensity shows a larger increase with Re_τ in comparison with the axial component. The position of this peak is moving further away from the wall with Re_τ for $u_{r,rms}^+$ while it is located around $y^+ = 40$ for $u_{\theta,rms}^+$. For the only non-vanishing Reynolds shear stress $\langle u_z u_r \rangle^+$, it can

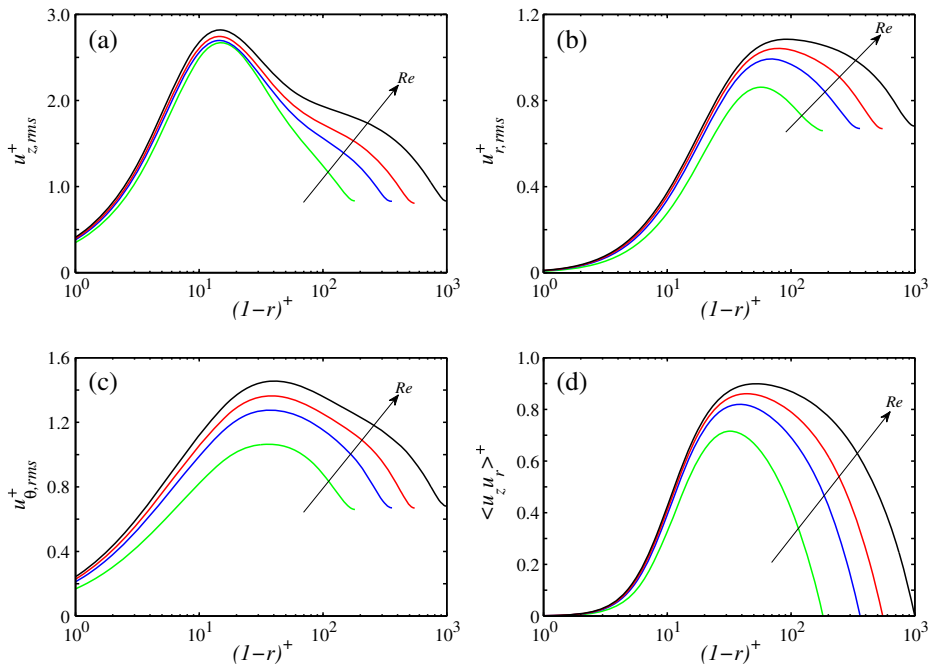


Fig. 7 Turbulence intensities and Reynolds shear stress in inner scaling as a function of $(1-r)^+$. **a** Axial, $u_{z,rms}^+$; **b** radial, $u_{r,rms}^+$; **c** azimuthal, $u_{\theta,rms}^+$; **d** Reynolds shear stress, $\langle u_z u_r \rangle^+$

also be seen that the inner scaling with u_τ^2 is limited to a small region ($y^+ \lesssim 15$). Moreover, the peak in this component is slowly approaching unity for increasing Re_τ .

DNS data of turbulent boundary layers have been assessed extensively by Schlatter and Örlü [27] who highlighted systematic differences between these data sets by calculating, among other quantities, the deviation of the mean streamwise velocity profile from the modified Musker profile proposed by Chauhan et al. [3]. This deviation is displayed in Fig 8a for pipes, channels and boundary layers at $Re_\tau \approx 1,000$. The three canonical wall-bounded flows show a rather different behaviour. While the data for channel from Jiménez and Hoyas [13] and Lenaers et al. [18] are in very good mutual agreement, the three pipe-flow data sets presented here are surprisingly different from each other; in particular clear negative values close to the wall are only visible in the data set by Wu and Moin [36]. This comparison suggests that there are some non-physical discrepancies between the various pipe flow data sets, which should be investigated in more detail.

The log-law indicator function

$$\Xi = y^+ \frac{dU_z^+}{dy^+} \quad (4)$$

is shown in Fig. 8b, evaluated at $Re_\tau \approx 1,000$. It is apparent that in the near-wall region up to about $y^+ \approx 30$ the curves pertaining to the various flow cases (pipe, channel, boundary layers) agree very well. Only upon reaching the first minimum in Ξ at $y^+ \approx 70$, the pipe flow data appears to be slightly higher, $\Xi = 2.329$, as opposed

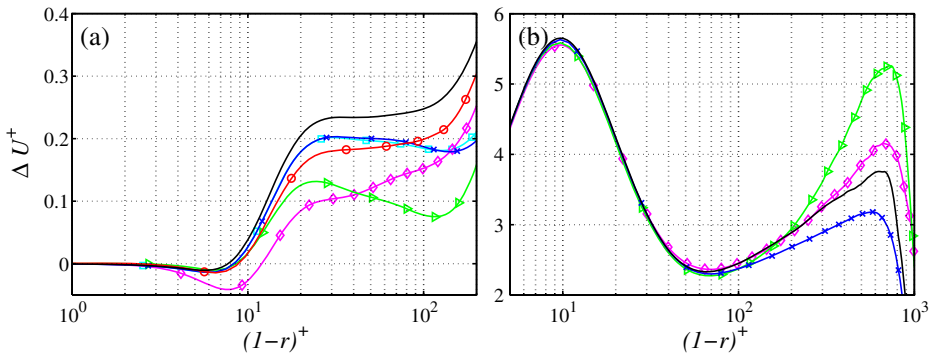


Fig. 8 **a** Deviation of the mean axial/streamwise velocity profile from the modified Musker profile (Chauhan et al. [3]) as a function of $(1-r)^+$ at $Re_\tau \approx 1,000$. **b** Log-law indicator function $(1-r)^+ dU_z^+/d(1-r)^+$ at $Re_\tau \approx 1,000$. *Pipe*: —, present DNS; —○—, Klewicky et al. [17]; —◇—, Wu and Moin [36]; *channel*: —×—, Lenaers et al. [18]; —□—, Jiménez and Hoyas [13]; *boundary layer*: —▷—, Schlatter and Örlü [27]

to channels and boundary layers, $\Xi = 2.299$ and 2.284 ; this minute but systematic difference is thought to be genuine and not an effect of limited sampling. When going further away from the wall, for high Reynolds numbers Ξ is expected to reach a plateau, indicating the existence of a logarithmic region in which $\Xi = \kappa^{-1}$. For the present cases, however, the Reynolds number is fairly low and no such plateau is visible. In addition, all curves depart when approaching the wake region. Naturally, the boundary layer exhibits the largest gradient due to the intermittent outer region, followed by the pipe and channel flows, as discussed above.

To further highlight the need for accurate DNS of turbulent pipe flows, various statistical moments of the axial/streamwise velocity, evaluated in the pipe centre, are shown in Fig. 9. For comparison, channel-flow data are also included, evaluated in the centre plane. It is worthwhile to note that the statistical average in pipes gets increasingly demanding as the centreline is approached due to the decrease in the circumferential length. Eventually, one point only remains in the centre indicating that the statistical data is averaged in time and axial direction only. This is not the case for channel or boundary-layer geometries. Together with the numerical difficulties in treating the singularity at the centreline, we can expect that evaluating higher-order statistical moments in the pipe centre can be used to determine the accuracy and level of convergence of simulations and experiments alike. Figure 9a shows the axial/streamwise fluctuations $u_{z,rms}^+$ over a range of friction Reynolds numbers and simulations. From the channel data, a weakly increasing trend can be established, whereas the data by Wu and Moin [36] in the pipe indicates an equally weak decreasing trend. Chin's [5] and Klewicky's [17] results, however, appear to be fairly constant, which is approximately confirmed by our own data. The skewness and flatness factors, Fig. 9b and c, are only provided by our own data sets in pipe and channel, and show nearly constant values with $S \approx -0.48$ and $F \approx 3.4$. Channels exhibit a similar constant trend, but at slightly different values $S \approx -0.57$ and $F \approx 3.55$. The fluctuations are thus weakly non-normally distributed in the centre of the two flow configurations.

The variation of the inner scaled maximum axial turbulence intensity in the near-wall region is shown in Fig. 10 as a function of the friction Reynolds number

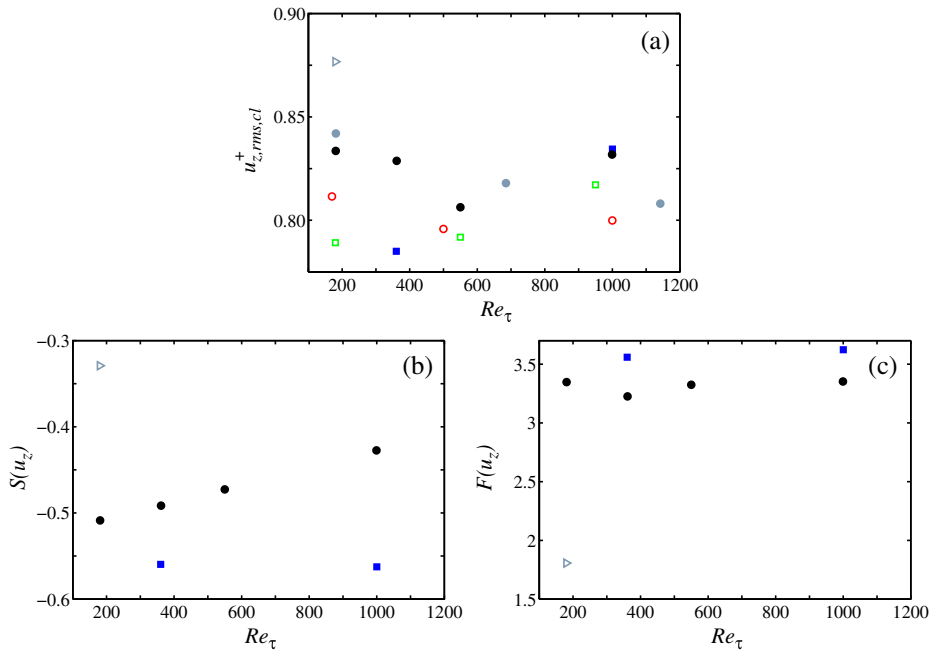


Fig. 9 Various statistical quantities at the centre of pipe and channel. **a** Axial turbulence intensity, $u_{z,rms}^+$; **b** skewness, $S(u_z)$; **c** flatness, $F(u_z)$. *Pipe*: \bullet , present DNS; \circ , Chin et al. [5], Klewicki et al. [17]; \bullet , Wu and Moin [36], Wu et al. [35]; \triangleright , Eggels et al. [8]. *Channel*: \blacksquare , in-house DNS, Lenaers et al. [18]; \square , Jiménez and Hoyas [13]

for the canonical wall-bounded flows. It is clearly observed that the maximum in axial/streamwise intensity increases with Re_τ for pipes, channels and boundary layers with an obvious discrepancy between pipes and the other two flow cases; the data from Jiménez and Hoyas [13], Lenaers et al. [18] and Schlatter and Örlü

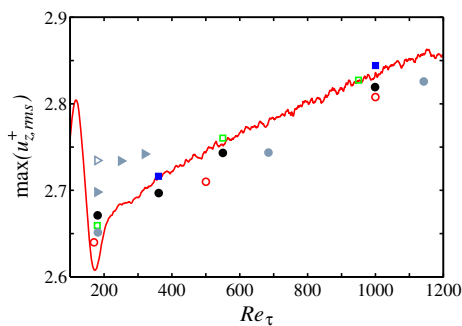


Fig. 10 Maximum of inner scaled axial turbulence intensity $u_{z,rms}^+$ as a function of the friction Reynolds number Re_τ . *Pipe*: \bullet , present DNS; \circ , Chin et al. [5], Klewicki et al. [17]; \bullet , Wu and Moin [36], Wu et al. [35]; \triangleright , Wagner et al. [33]; \triangleright , Eggels et al. [8]. *Channel*: \blacksquare , in-house DNS, Lenaers et al. [18]; \square , Jiménez and Hoyas [13]. *Boundary layer*: —, Schlatter and Örlü [27]

[27] for channels and boundary layer are in good agreement and higher than that for pipes. This increase in the inner near wall peak is due to the growth of the large scale structures with Re_τ in the logarithmic layer as mentioned above; see for instance del Álamo and Jiménez [7]. Meanwhile, the influence of the outer layer large scale structures on the wall was studied by Örlü and Schlatter [26] for turbulent boundary layers and was manifested by the Reynolds number dependence of the axial/streamwise wall-shear stress ($\tau_{z,rms}^+$). This can be seen in Fig. 11 where $\tau_{z,rms}^+$ and the azimuthal component ($\tau_{\theta,rms}^+$) are displayed together with DNS data of Schlatter and Örlü [27] and Jiménez and Hoyas [12] for turbulent boundary layer and channel flow, respectively. In a similar trend as for $\max(u_{z,rms}^+)$, these quantities increase with Re_τ for the three canonical flows. In this case, however, the boundary layer gives higher values than channels and pipe which are nearly equal. It is thus interesting to note that for $\tau_{z,rms}^+$ channels and pipes agree very well (at the same Re_τ), but not in the fluctuation maximum $u_{z,rms}^+$. One may speculate that the higher wall shear fluctuations in boundary layers are due to higher pressure fluctuation intensity in the outer region caused by the intermittency with potential flow. In order to have a look at the pressure behaviour in this case, the mean pressure, rms of pressure fluctuation and its maximum as well as its value at the wall are displayed in Figs. 12 and 13. The mean pressure P^+ shows a rather different behaviour in the outer region of the three canonical flow cases with P^+ being substantially lower in the wake of pipe flow in comparison to channel and boundary layer flow. This is directly related to the differences in the wall-normal turbulence intensity. The mean radial momentum equation in pipe flow reads

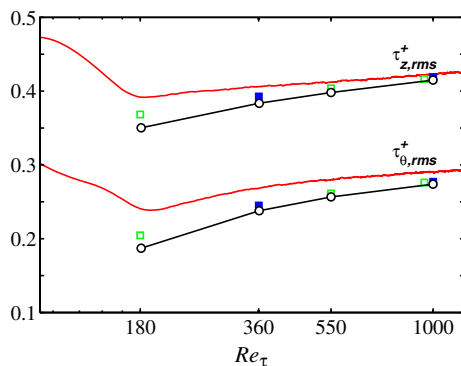
$$\frac{1}{\rho} \frac{\partial P}{\partial r} + \frac{d}{dr} \langle u_r u_r \rangle + \frac{\langle u_r u_r \rangle - \langle u_\theta u_\theta \rangle}{r} = 0. \quad (5)$$

By changing variable such that the above equation starts from the wall and then integrating, it can be shown that the mean pressure in pipes is expressed by

$$P^+(r) = -\langle u_r u_r \rangle^+ - f(r), \quad (6)$$

where $f(r)$ is a positive function that increases with r and is zero at the wall. In channel and boundary layer flows, the mean pressure is balanced by the wall-normal fluctuations; i.e. $P^+ + \langle vv \rangle^+ = 0$ with P^+ set to zero at the wall. It is worthwhile to

Fig. 11 Axial/streamwise ($\tau_{z,rms}^+$) and azimuthal/spanwise ($\tau_{\theta,rms}^+$) fluctuating shear stresses as a function of the friction Reynolds number Re_τ . Pipe: \circ —, present DNS; channel: \blacksquare , in-house DNS, Lenaers et al. [18]; \square , Jiménez and Hoyas [13]; —, boundary layer: Schlatter and Örlü [27]



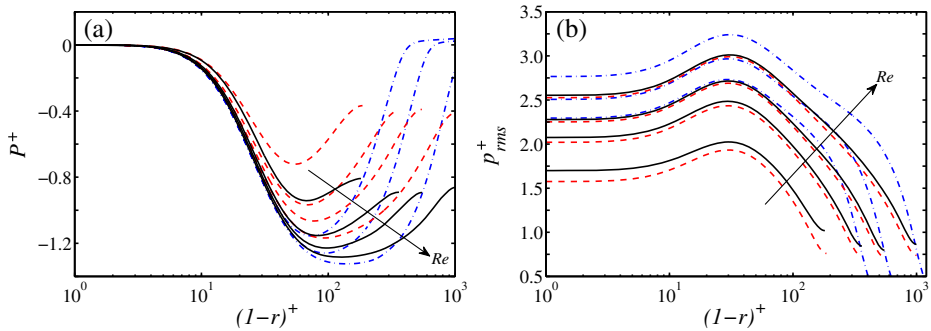


Fig. 12 **a** Mean pressure as a function of $(1-r)^+$. **b** Root mean square of pressure fluctuation p_{rms}^+ . Pipe: —, present DNS; channel: ---, Jiménez and Hoyas [13] ($Re_\tau = 180, 550$), in-house DNS ($Re_\tau = 360$), Lenaers et al. [18] ($Re_\tau = 1,000$); boundary layer: - · -, Schlatter and Örlü [27] ($Re_\tau = 360, 550, 974$)

note that the mean wall-normal momentum equation for boundary layer contains several terms that are associated with the streamwise gradients, wall-normal mean velocity and viscous effects. However, these terms are negligible in comparison to the wall-normal gradient of $\langle vv \rangle^+$. Since the wall-normal turbulence intensity is higher in pipe flow than in channel flow $\langle u_r u_r \rangle^+ > \langle vv \rangle^+$, the mean pressure for pipe flow is lower. The same applies between boundary layer and channel flows whereas the extra term $f(r)$ in Eq. 6 results in a lower pressure in pipes with respect to boundary layers. The maximum of p_{rms}^+ and its value at the wall, displayed in Eq. 13, shows the same Reynolds number dependence as the fluctuating wall shear stresses. Pipe and channel flows match and have lower values than the boundary layer. The overall behaviour indicates that pipes and channels are similar in the near wall region, apart from the maximum inner peak in $u_{z,rms}^+$, but are different in the wake.

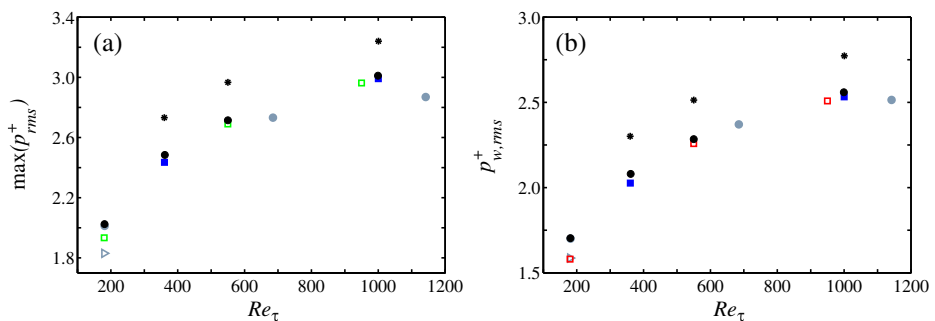


Fig. 13 **a** Maximum of inner scaled root mean square of pressure fluctuations p_{rms}^+ . **b** p_{rms}^+ at the wall ($p_{w,rms}^+$). Pipe: •, present DNS; •, Wu and Moin [36], Wu et al. [35]; ▷, Eggels et al. [8]. Channel: ■, in-house DNS, Lenaers et al. [18]; □, Jiménez and Hoyas [13]. Boundary layer: *, Schlatter and Örlü [27]

4.3 Turbulent kinetic energy

The turbulent kinetic energy (TKE) budget is half the sum of the diagonal terms of the Reynolds stress budget and is given by

$$\frac{Dk}{Dt} = P^k + \varepsilon + \Pi^k + D^k + T^k \quad (7)$$

where $k = (\langle u_r^2 \rangle + \langle u_\theta^2 \rangle + \langle u_z^2 \rangle)/2$ and the right-hand side of the above equation is identified as: $P^k = -\langle u_i u_j \rangle \partial U_i / \partial x_j$: production; $\varepsilon = -\nu \langle \partial u_i / \partial x_j \partial u_i / \partial x_j \rangle$: viscous dissipation; $\Pi^k = -(1/\rho) \partial \langle p u_i \rangle / \partial x_i$: pressure-related diffusion; $D^k = (\nu/2) \partial^2 \langle u_i u_i \rangle / \partial x_j^2$: viscous diffusion and $T^k = -(1/2) \partial \langle u_i u_i u_j \rangle / \partial x_j$: turbulent velocity related diffusion, respectively. The mean advection term is zero and only present in boundary layer flows. The TKE budget for the present simulations for $Re_\tau = 180, 360$ and 550 are shown in Figs. 14a, b and c and for $Re_\tau = 1,000$ together with that for channels and boundary layers in Fig. 14d. The sum of all terms in the TKE equation is of the order 10^{-4} in plus units indicating that all terms are sufficiently converged. The overall behaviour of the budget terms at the different Reynolds number is very similar and

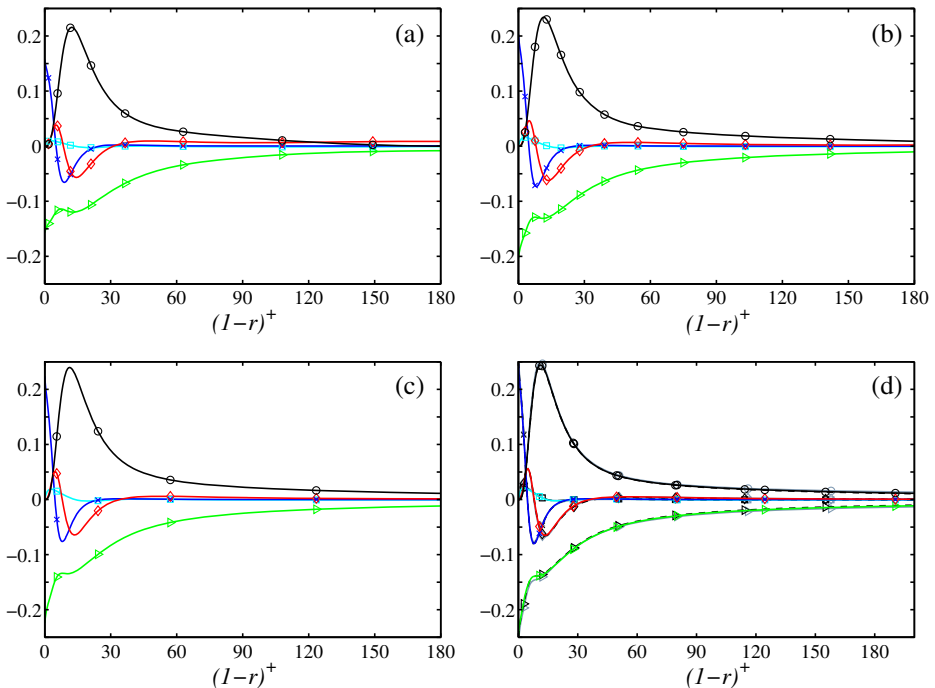


Fig. 14 Turbulent kinetic energy budget normalised by u_τ^4/ν . **a** Pipe, $Re_\tau = 180$; **b** pipe, $Re_\tau = 360$; **c** pipe, $Re_\tau = 550$; **d** $Re_\tau = 1,000$; pipe: —, present DNS; channel: ----, Lenaers et al. [18]; boundary layer: (grey), Schlatter and Örlü [27]; the profiles for the three canonical cases are indistinguishable at this Re_τ . —○—, Production P^k ; —△—, viscous dissipation ε ; —□—, pressure-related diffusion Π^k ; —×—, viscous diffusion D^k ; —◇—, turbulent velocity related diffusion T^k

at $Re_\tau = 1,000$ the TKE budgets for the pipe, channel and boundary layer are almost indistinguishable in the near-wall region. The budget is dominated by production and viscous dissipation where the expected large peak of positive production (asymptotic value = 0.25) is observed in the buffer layer just below the position of maximum $u_{z,rms}$; i.e. $(1-r)^+ = 15$. In the same region, the ratio of production to viscous dissipation is larger than unity, and a balance is obtained due to the presence of negative turbulent and viscous diffusion. These terms extract energy from this layer and transport it away from the buffer region. Very close to the wall, the major contribution to the TKE budget comes from the viscous diffusion and dissipation terms. In the outer layer, the effect of most of the TKE terms essentially vanish, except for production and viscous dissipation, which tend to be in balance.

While the TKE budget in the local inner layer is studied by means of inner scaling in the previous figure, the terms in the outer layer can be highlighted through the premultiplied budget. Plotted with logarithmic abscissa, the apparent area below the curves between two wall-normal positions directly corresponds to the integral of the various budget terms. Note that for the pipe the premultiplication contains two terms; one related to the integration along a logarithmic abscissa, $(1-r)^+$, and one coming from the circular geometry, r . In channels and boundary layers, however, only the inner-scale wall distance, y^+ enters in the premultiplication. In Fig. 15a, pipes, channels and boundary layers are compared at $Re_\tau \approx 1,000$. As previously discussed, the near-wall region is characterised by a nearly perfect agreement of all cases. Differences start to appear after $(1-r)^+ \approx 100$, coinciding with the onset of change in the gradient of the velocity profiles as discussed in Fig. 8b above. The premultiplied production attains its highest value in the wake region for the boundary layer, clearly linked to the intermittent flow and the thus more rapidly increasing mean velocity. The various transport terms are comparably small even in the first part of the outer region (up to about $y/R \approx 0.5$), and the dissipation is increased in accordance with production. Towards the centre (or towards the boundary-layer edge) the production goes to zero due to the vanishing velocity gradient, while the dissipation reaches finite values for channels and pipes, balanced by turbulent

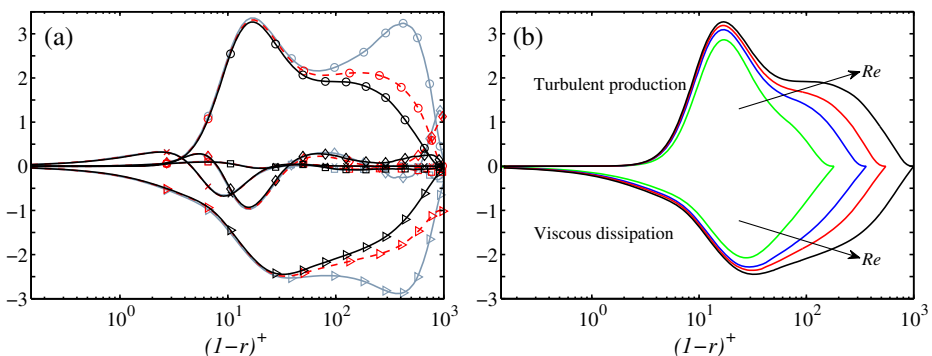


Fig. 15 Premultiplied turbulent kinetic energy budget normalised by u_τ^4/ν . Premultiplication in pipe $r(1-r)^+$; in channels and boundary layers y^+ . **a** $Re_\tau = 1,000$; *pipe*: —, present DNS; *channel*: - - -, Lenaers et al. [18]; *boundary layer*: — (grey), Schlatter and Örlü [27]. —○—, Production P^k ; —□—, viscous dissipation ε ; —□—, pressure-related diffusion Π^k ; —×—, viscous diffusion D^k ; —◇—, turbulent velocity related diffusion T^k . **b** Effect of Reynolds number in pipes

diffusion. In the case of the boundary layer, mean advection is also non-vanishing in that region, allowing both production and dissipation to go to low values.

The effect of Reynolds number on the premultiplied TKE budget for pipes is demonstrated in Fig. 15b where the most dominant terms are shown; production and viscous dissipation. The Reynolds number is still too low to allow for a final conclusion regarding the high- Re behaviour in pipes; see e.g. Smits et al. [30]. It is clear that there is no outer peak in the premultiplied production and dissipation terms. This is a consequence of including the geometry factor r in the premultiplication; without that factor the pipe would actually show a peak slightly lower than the boundary layer. The behaviour in the inner region, up to $(1 - r)^+ \approx 30$, is however nearly the same for the present (limited) range of Reynolds numbers. Furthermore, it can be observed that the case corresponding to the lowest $Re_\tau = 180$ shows noticeable differences even near the wall, indicating the presence of dominant low-Reynolds-number effects. Therefore, this case should be excluded when discussing scalings towards higher Re .

5 Conclusions

DNS of fully developed turbulent pipe flow has been performed at moderately high Reynolds numbers, ranging from $Re_\tau = 180$ to 1,000, based on friction velocity and pipe radius R . The axial extent of the domain is chosen $25R$ which can be considered sufficiently long to represent all the relevant structures present in this case. The incompressible Navier–Stokes equations are solved numerically in a Cartesian system, and the difficulties associated with numerical singularity in the pipe centre arising from cylindrical coordinates are thus avoided. Low and high-order moments in addition to the complete Reynolds-stress budgets are obtained. The underlying discretisation is the spectral-element method (SEM), implemented in the highly parallel code `nek5000`, allowing for high spatial order and favourable dispersion properties coupled with numerical efficiency. The quality of the mesh has been chosen fine to resolve the relevant turbulent fluctuations. In particular the instantaneous fields of axial vorticity showed no effect of the non-equidistant discretisation on spectral elements.

The new pipe data is extensively compared to other simulation data pertaining to pipes, channels and boundary layers; channel data include both in-house data sets and literature data. In a first step, the various available DNS data in the literature for pipes at similar Reynolds numbers are critically assessed. Recall that in pipe flow the only parameter apart from the Reynolds number is the length of the considered pipe. Once this axial extent is chosen large enough, all data should in principle be the same. Small, but still substantial and systematic differences between the various data sets even in the mean flow profile (for instance highlighted via log-law diagnostic function or the difference to analytical velocity profiles) suggest non-physical discrepancies between these simulations and are thus highlighting the need for high-order accurate methods for this particular flow case.

The variation of velocity and pressure fluctuations with the Reynolds number showed a clear dependency on Re for pipes, channels, and boundary layers. Comparing the data in more detail, most of the mean and fluctuation profiles show a high degree of similarity between all these canonical wall flows, as expected. Distinct

differences appearing mainly in the wake region, as expected, are highlighted. Also, the pressure, both for the mean and fluctuation, shows a non-trivial dependency on the flow case: Scaled in inner units, the mean pressure turns out to be lowest in pipes due to the presence of radial and azimuthal Reynolds stresses in the radial mean momentum equation. On the other hand, the pressure fluctuations throughout the profile for the two internal flows are very similar, and about 10% lower than in the boundary layer.

Considering the velocity fluctuations in the inner region, other interesting discrepancies between the canonical flows can be established. For instance, the maximum of the axial fluctuations in the buffer region seems to be on the same level for channels and boundary layers (comparing them at the same Re_τ), and distinctly higher than in pipes for sufficiently high Re . However, the fluctuations of both axial and azimuthal wall shear stress clearly are in the boundary layer more intense than the internal flows. The origin and physical mechanisms responsible for this behaviour is still unclear. Finally, budgets of the turbulent kinetic energy are evaluated and compared. As expected, the inner region is virtually independent of the flow case (up to $y^+ \approx 100$), but the wake region features the largest differences.

Acknowledgements Computer time on Lindgren was granted by The Swedish National Infrastructure for Computing (SNIC) and on HECToR by PRACE through the DECI project PIPETURB. We would also like to thank the Göran Gustafsson Foundation for the financial support. Development of the nek5000 algorithm is supported by the U.S. Department of Energy Applied Mathematics Research Program. Financial support from the Swedish Research Council VR (2010 – 4147, 2010 – 6965), is gratefully acknowledged.

References

1. Alfredsson, P.H., Segalini, A., Örlü, R.: A new scaling for the streamwise turbulence intensity in wall-bounded turbulent flows and what it tells us about the “outer” peak. *Phys. Fluids* **23**, 041702 (2011)
2. Boersma, B.J.: Direct numerical simulation of turbulent pipe flow up to a Reynolds number of 61,000. *J. Phys.* **318**, 042045 (2011)
3. Chauhan, K.A., Monkewitz, P.A., Nagib, H.M.: Criteria for assessing experiments in zero pressure gradient boundary layers. *Fluid Dyn. Res.* **41**, 021404 (2009)
4. Chevalier, M., Schlatter, P., Lundbladh, A., Henningson, D.S.: SIMSON—A pseudo-spectral solver for incompressible boundary layer flows. Tech. Rep. TRITA-MEK 2007:07, KTH Mechanics, Stockholm, Sweden (2007)
5. Chin, C., Ooi, A.S.H., Marusic, I., Blackburn, H.M.: The influence of pipe length on turbulence statistics computed from direct numerical simulation data. *Phys. Fluids* **22**, 115107 (2010)
6. Coles, D.: The law of the wake in the turbulent boundary layer. *J. Fluid Mech.* **1**, 191–226 (1956)
7. del Álamo, J.C., Jiménez, J.: Spectra of the very large anisotropic scales in turbulent channels. *Phys. Fluids* **15**, L41–L44 (2003)
8. Eggels, J.G.M., Unger, F., Weiss, M.H., Westerweel, J., Adrian, R.J., Friedrich, R., Nieuwstadt, F.T.M.: Fully developed turbulent pipe flow: a comparison between direct numerical simulation and experiment. *J. Fluid Mech.* **268**, 175–209 (1994)
9. Fischer, P.F., Lottes, J.W., Kerkemeier, S.G.: nek5000 web page. <http://nek5000.mcs.anl.gov> (2008)
10. Fukagata, K., Kasagi, N.: Highly energy-conservative finite difference method for the cylindrical coordinate system. *J. Comput. Phys.* **181**, 478–498 (2002)
11. Guala, M., Hommema, S.E., Adrian, R.J.: Large-scale and very-large-scale motions in turbulent pipe flow. *J. Fluid Mech.* **554**, 521–542 (2006)
12. Hoyas, S., Jiménez, J.: Reynolds number effects on the Reynolds-stress budgets in turbulent channels. *Phys. Fluids* **20**, 101511 (2008)

13. Jiménez, J., Hoyas, S.: Turbulent fluctuations above the buffer layer of wall-bounded flows. *J. Fluid Mech.* **611**, 215–236 (2008)
14. Jiménez, J., Hoyas, S., Simens, M.P., Mizuno, Y.: Turbulent boundary layers and channels at moderate Reynolds numbers. *J. Fluid Mech.* **657**, 335–360 (2010)
15. Kim, J., Moin, P., Moser, P.: Turbulence statistics in fully developed channel flow at low Reynolds number. *J. Fluid Mech.* **177**, 133–166 (1987)
16. Kim, K.C., Adrian, R.J.: Very large-scale motion in the outer layer. *Phys. Fluids* **11**, 417–422 (1999)
17. Klewicki, J., Chin, C., Blackburn, H.M., Ooi, A., Marusic, I.: Emergence of the four layer dynamical regime in turbulent pipe flow. *Phys. Fluids* **24**, 045107 (2012)
18. Lenaers, P., Li, Q., Brethouwer, Schlatter, P., Örlü, R.: Rare backflow and extreme wall-normal velocity fluctuations in near-wall turbulence. *Phys. Fluids* **24**, 035110 (2012)
19. Maday, Y., Patera, A.: Spectral element methods for the Navier–Stokes equations. In: Noor, A.K. (ed.) *State of the Art Surveys in Computational Mechanics* ASME, pp. 71–143 (1989)
20. Marusic, I., McKeon, B.J., Monkewitz, P.A., Nagib, H.M., Smits, A.J.: Wall-bounded turbulent flows at high Reynolds numbers: recent advances and key issues. *Phys. Fluids* **22**, 065103 (2010)
21. Monty, J.P., Stewart, J.A., Williams, R.C., Chong, M.S.: Large-scale features in turbulent pipe and channel flows. *J. Fluid Mech.* **589**, 147–156 (2007)
22. Moody, L.F.: Friction factors for pipe flow. *Trans. ASME* **66**, 671–684 (1944)
23. Nagib, H.M., Chauhan, K.A.: Variations of von Kármán coefficient in canonical flows. *Phys. Fluids* **20**, 101518 (2008)
24. Ohlsson, J., Schlatter, P., Mavriplis, C., Henningson, D.S.: The spectral-element method and the pseudo-spectral method—a comparative study. In: Rønquist, E. (ed.) *Lecture Notes in Computational Science and Engineering*, pp. 459–467. Springer, Berlin, Germany (2011)
25. Orlandi, P., Fatica, M.: Direct simulations of turbulent flow in a pipe rotating about its axis. *J. Fluid Mech.* **343**, 43–72 (1997)
26. Örlü, R., Schlatter, P.: On the fluctuating wall-shear stress in zero pressure-gradient turbulent boundary layer flows. *Phys. Fluids* **23**, 021704 (2011)
27. Schlatter, P., Örlü, R.: Assessment of direct numerical simulation data of turbulent boundary layers. *J. Fluid Mech.* **659**, 116–126 (2010)
28. Schlatter, P., Örlü, R.: Turbulent boundary layers at moderate Reynolds numbers: inflow length and tripping effects. *J. Fluid Mech.* **710**, 5–34 (2012)
29. Schlatter, P., Örlü, R., Li, Q., Brethouwer, G., Fransson, J.H.M., Johansson, A.V., Alfredsson, P.H., Henningson, D.S.: Turbulent boundary layers up to $Re_\theta = 2,500$ studied through simulation and experiment. *Phys. Fluids* **21**, 051702 (2009)
30. Smits, A.J., McKeon, B.J., Marusic, I.: High-Reynolds number wall turbulence. *Annu. Rev. Fluid Mech.* **43**, 353–375 (2011)
31. Spalart, P.R.: Direct simulation of a turbulent boundary layer up to $Re_\theta = 1410$. *J. Fluid Mech.* **187**, 61–98 (1988)
32. Talamelli, A., Persiani, F., Fransson, J.H.M., Alfredsson, P.H., Johansson, A., Nagib, H.M., Rüedi, J., Sreenivasan, K.R., Monkewitz, P.A.: CICLoPE—a response to the need for high Reynolds number experiments. *Fluid Dyn. Res.* **41**, 1–22 (2009)
33. Wagner, C., Hüttl, T.J., Friedrich, R.J.: Low-Reynolds-number effects derived from direct numerical simulations of turbulent pipe flow. *Comp. Fluids* **30**, 581–590 (2001)
34. Walpot, R.J.E., van der Geld, C.W.M., Kuerten, J.G.M.: Determination of the coefficients of langevin models for inhomogeneous turbulent flows by three-dimensional particle tracking velocimetry and direct numerical simulation. *Phys. Fluids* **19**, 045102 (2007)
35. Wu, X., Baltzer, J.R., Adrian, R.J.: Direct numerical simulation of a 30R long turbulent pipe flow at $R^+ = 685$: large- and very large-scale motions. *J. Fluid Mech.* **698**, 235–281 (2012)
36. Wu, X., Moin, P.: A direct numerical simulation study on the mean velocity characteristics in turbulent pipe flow. *J. Fluid Mech.* **608**, 81–112 (2008)
37. Zagarola, M.V., Smits, A.J.: Scaling of the mean velocity profile for turbulent pipe flow. *Phys. Rev. Lett.* **78**, 239–242 (1997)